







## An atomically tailored chiral magnet with small skyrmions at room temperature

Tao Liu<sup>1,6</sup>, Camelia M. Selcu<sup>1,6</sup>, Binbin Wang<sup>2,3</sup>, Núria Bagués<sup>2,3</sup>, Po-Kuan Wu<sup>1</sup>, Timothy Q. Hartnett<sup>4</sup>, Shuyu Cheng<sup>1</sup>, Denis Pelekhov<sup>1</sup>, Roland A. Bennett<sup>1</sup>, Joseph Perry Corbett<sup>1</sup>, Jacob R. Repicky <sup>1</sup>, Brendan McCullian <sup>1</sup>, P. Chris Hammel<sup>1</sup>, Jay A. Gupta <sup>1</sup>, Mohit Randeria<sup>1</sup>, Prasanna V. Balachandran <sup>4,5</sup>, David W. McComb <sup>2,3</sup> & Roland K. Kawakami <sup>1</sup> ✉

Creating materials that do not exist in nature can lead to breakthroughs in science and technology. Magnetic skyrmions are topological excitations that have attracted great attention recently for their potential applications in low power, ultrahigh density memory. A major challenge has been to find materials that meet the dual requirement of small skyrmions stable at room temperature. Here we meet both these goals by developing epitaxial FeGe films with excess Fe using atomic layer molecular beam epitaxy (MBE) far from thermal equilibrium. Our atomic layer design permits the incorporation of 20% excess Fe while maintaining a non-centrosymmetric crystal structure supported by theoretical calculations and necessary for stabilizing skyrmions. We show that the Curie temperature is well above room temperature, and that the skyrmions have sizes down to 15 nm as imaged by Lorentz transmission electron microscopy (LTEM) and magnetic force microscopy (MFM). The presence of skyrmions coincides with a topological Hall effect-like resistivity. These atomically tailored materials hold promise for future ultrahigh density magnetic memory applications.

<sup>1</sup>Department of Physics, The Ohio State University, Columbus, OH 43210, USA. <sup>2</sup>Center for Electron Microscopy and Analysis, The Ohio State University, Columbus, OH 43212, USA. <sup>3</sup>Department of Materials Science and Engineering, The Ohio State University, Columbus, OH 43210, USA. <sup>4</sup>Department of Materials Science and Engineering, University of Virginia, Charlottesville, VA 22902, USA. <sup>5</sup>Department of Mechanical and Aerospace Engineering, University of Virginia, Charlottesville, VA 22902, USA. <sup>6</sup>These authors contributed equally: Tao Liu, Camelia M. Selcu. ✉email: [kawakami.15@osu.edu](mailto:kawakami.15@osu.edu)

**M**agnetic skyrmions are a leading candidate for next-generation storage technology due to their potential for combining topological stability, small size, and room temperature operation along with low energies for moving or writing skyrmions<sup>1–5</sup>. In contrast to conventional magnetic storage where the transition from ferromagnetism to superparamagnetism limits the size reduction of data bits, topological skyrmions are not subject to this restriction so there is tremendous interest in reducing skyrmion size at room temperature. However, it is challenging to find materials that can generate skyrmions at room temperature with a size below 20 nm, which is a major bottleneck for their development<sup>6,7</sup>. B20 materials such as FeGe and MnGe are among the most widely studied skyrmion materials<sup>8–21</sup> and show promising characteristics such as small size at low temperatures (~3 nm in MnGe<sup>19,20</sup>) and Curie temperatures above room temperature for some materials<sup>21,22</sup>. However, the combination of small skyrmion size with stability at room temperature remains elusive.

We start from FeGe which has a Curie temperature just below room temperature (~280 K) and a skyrmion size of ~80 nm<sup>12–18</sup>. Our strategy is to incorporate excess Fe to increase the Curie temperature while maintaining the non-centrosymmetric structure to maintain the bulk Dzyaloshinskii–Moriya interaction (DMI)<sup>23,24</sup> which gives rise to the twisting skyrmion spin texture (Fig. 1a). To this end, we develop Fe-rich Fe<sub>1.2</sub>Ge using atomic layer MBE (ALMBE) where Fe and Ge atomic layers are deposited sequentially in accordance with the layered structure of FeGe(111) (Fig. 1b). Under highly nonequilibrium conditions, we demonstrate the incorporation of 20% excess Fe within the B20 crystal structure to produce Fe<sub>1.2</sub>Ge, which increases the Curie temperature to above 400 K. In terms of structure, there is no evidence of secondary phases in the transmission electron microscopy (TEM) and X-ray diffraction (XRD) results. This is supported by density functional theory (DFT) calculations showing the preferential incorporation of excess Fe atoms near specific atomic planes. Skyrmions with sizes down to 15 nm are imaged at room temperature using magnetic force microscopy (MFM) and Lorentz TEM (LTEM). The presence of skyrmions coincides with a topological Hall effect-like resistivity. These results confirm the presence of small skyrmions at room temperature in atomically tailored Fe-rich Fe<sub>1.2</sub>Ge.

## Results and discussion

**Material synthesis, structural analysis, and magnetic characterization.** We developed Fe-rich Fe<sub>1.2</sub>Ge using MBE growth on top of a pure FeGe buffer layer on Si(111) (see Methods for details of MBE growth) and structural characterization by reflection high energy electron diffraction (RHEED) (Fig. 2a), XRD (Fig. 2b) and TEM (Fig. 2c). Attempts to incorporate excess Fe atoms into FeGe using conventional MBE by co-deposition of Fe and Ge at 300 °C led to phase separation and creation of secondary phases. This can be seen by the presence of extra peaks in the XRD scan for Fe<sub>1.2</sub>Ge by co-deposition (green curve of Fig. 2b) and the formation of rings in the RHEED pattern (lower left image of Fig. 2a) that do not appear for pure FeGe (upper left image of Fig. 2a). Attempts to incorporate excess Fe by co-deposition within the typical growth temperature window for FeGe of 200–350 °C have failed.

As an alternative, we employed ALMBE to sequentially deposit Fe and Ge atomic layers according to the layered structure along [111] (Fig. 1b, side view) with repetitions of Ge-sparse, Fe-sparse, Ge-dense, and Fe-dense layers. As shown in Fig. 1b (top view), the dense layers have a three-atom basis on a hexagonal lattice, and the sparse layers have a one-atom basis on a hexagonal lattice<sup>25</sup>. The growth of stoichiometric FeGe by ALMBE proceeded successfully over an expanded growth temperature window down to room temperature (RT), where the RHEED pattern is streaky (upper right image of Fig. 2a) but slightly wider than for conventional growth (upper left image of Fig. 2a). Under these high nonequilibrium conditions, we grew Fe-rich Fe<sub>1.2</sub>Ge using RT-ALMBE by increasing the growth time of the Fe-sparse layer by 80%. We observed no discernible changes in the RHEED pattern (lower right image of Fig. 2a) compared to stoichiometric FeGe and no obvious signs of secondary phases appeared. This is further supported by XRD scans (red curve, Fig. 2b) which show no additional peaks compared to pure FeGe (blue curve, Fig. 2b). The one notable difference is that the B20 FeGe peak has a slight shift to lower angles (Fig. 2b inset) which indicates that the Fe-rich Fe<sub>1.2</sub>Ge has a 0.5% expanded lattice parameter along the growth direction.

The atomic-scale structure of Fe-rich Fe<sub>1.2</sub>Ge was characterized by cross-sectional scanning (S)TEM. Figure 2c shows a STEM high-angle annular dark-field (HAADF) image of the interfacial

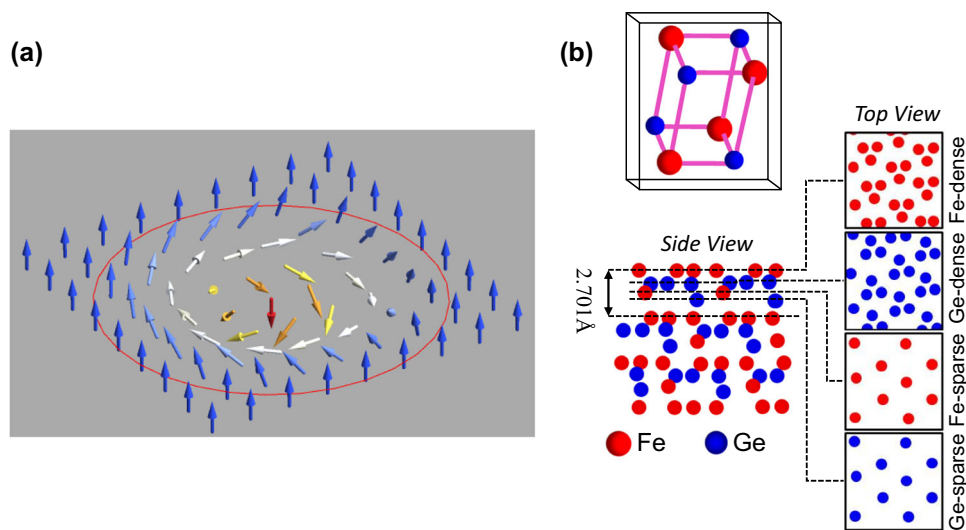


**Fig. 1 Skyrmions in B20 crystals.** **a** A schematic of a localized Bloch-type skyrmion spin texture. The arrows represent the magnetic moment and their colors represent the vertical component of the magnetization with blue as up and red as down. **b** Top: the atomic unit cell of FeGe with B20 crystal structure with broken inversion symmetry. Bottom: the atomic layer structure of FeGe for (111)-oriented films, showing a sequence of dense and sparse atomic layers of Fe and Ge.

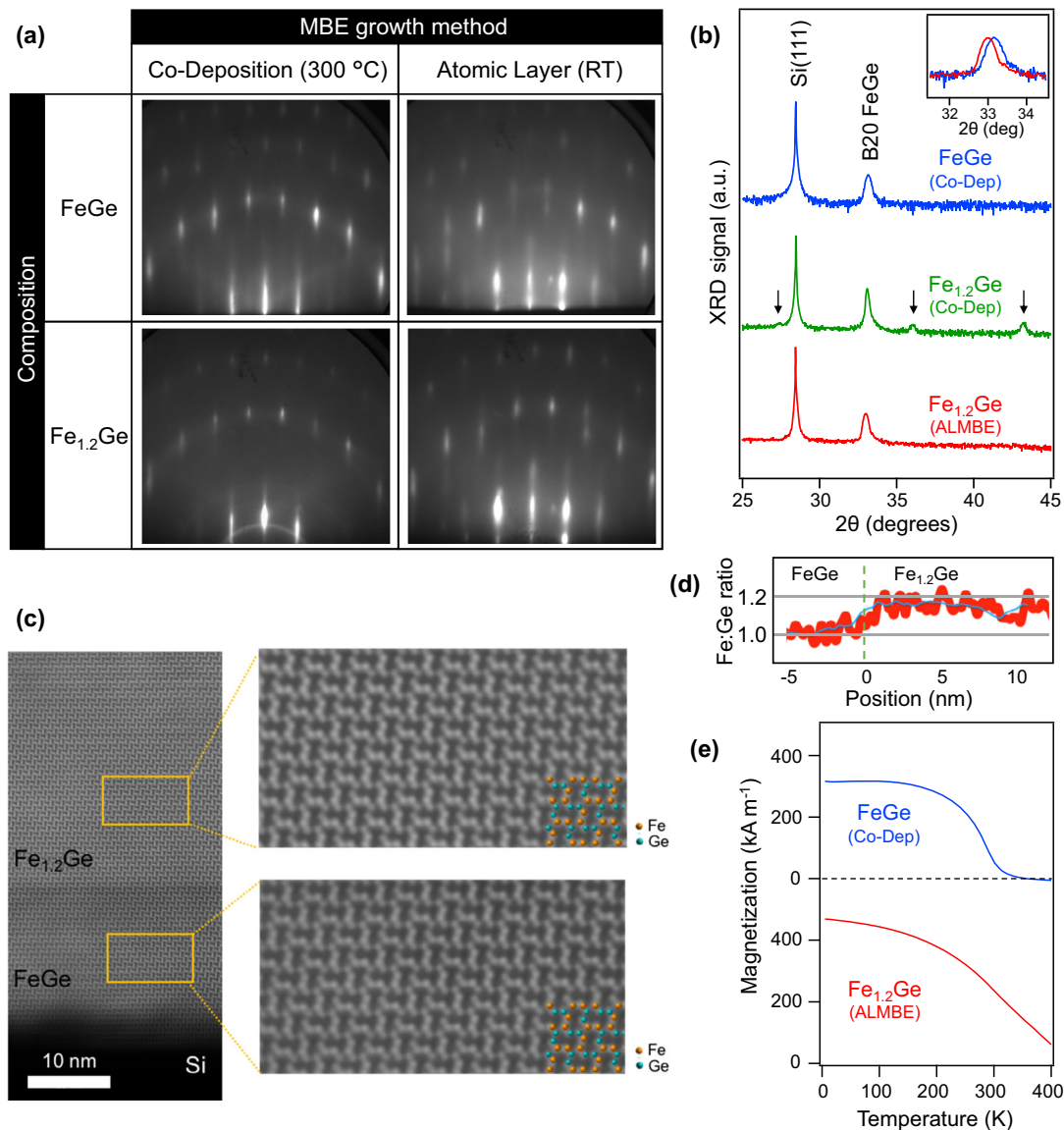


**Fig. 2 Growth, structure, and magnetic properties of Fe-rich Fe<sub>1.2</sub>Ge.** **a** Reflection high energy electron diffraction (RHEED) patterns for conventional FeGe co-deposited at 300 °C, Fe<sub>1.2</sub>Ge co-deposited at 300 °C, and FeGe and Fe<sub>1.2</sub>Ge grown by atomic layer molecular beam epitaxy (ALMBE) at room temperature. **b**  $\theta$ - $2\theta$  X-ray diffraction scans for co-deposited FeGe (blue curve), co-deposited Fe<sub>1.2</sub>Ge (green curve), and ALMBE Fe<sub>1.2</sub>Ge (red curve) show the presence of secondary phases (black arrows) for co-deposited Fe<sub>1.2</sub>Ge but not for ALMBE Fe<sub>1.2</sub>Ge. Inset: A close-up of the B20 FeGe peak for normal co-deposited FeGe (blue curve) and ALMBE Fe<sub>1.2</sub>Ge (red curve) indicates an expansion of the B20 lattice due to the incorporation of excess Fe. **c** Cross-sectional high angle annular dark-field scanning transmission electron microscopy (HAADF-STEM) image of Fe<sub>1.2</sub>Ge on FeGe/Si(111) showing the B20 lattice. **d** X-ray energy dispersive spectroscopy (XEDS) scan showing a higher Fe:Ge ratio in the Fe<sub>1.2</sub>Ge film. **e** Magnetization as a function of temperature with the out-of-plane field of 2 Tesla for FeGe (blue curve) and Fe-rich Fe<sub>1.2</sub>Ge (red curve).

region between the Fe<sub>1.2</sub>Ge film and the FeGe buffer. Most notable is the high quality of the Fe<sub>1.2</sub>Ge layer, which appears to be very similar to the FeGe buffer layer (grown at 300 °C). HAADF-STEM images also show the Fe-rich Fe<sub>1.2</sub>Ge film has grains of various sizes, from a few tens to few hundreds of nanometers, which reflects the size and orientation of the grains formed in the FeGe buffer layer<sup>26,27</sup>. Although the presence of the excess Fe is not apparent in the HAADF image, measurement of the composition using X-ray energy dispersive spectroscopy (XEDS) shows that the average Fe content in the Fe-rich Fe<sub>1.2</sub>Ge is 18% higher than in the FeGe buffer (Fig. 2d). Regarding the possible presence of secondary phases, neither the HAADF image nor the XEDS image provides any evidence for the formation of secondary phases or compositional inhomogeneity. Furthermore, the excess Fe is not resolved in the Fe-rich region in the atomic

resolution HAADF image, suggesting that they may have randomly occupied sites. This is supported by DFT calculations discussed next.

The ability to incorporate excess Fe atoms into the FeGe film was studied theoretically using DFT calculations of bulk FeGe with additional Fe atoms in the unit cell, where energy minimization was performed while allowing the lattice parameter along one of the [111] directions to vary (see Methods). With 12 Fe and 12 Ge atoms in the unit cell for the calculation, the addition of 1, 2, or 3 Fe atoms corresponds to an average excess Fe concentration of 8.3% (Fe<sub>1.08</sub>Ge), 16.7% (Fe<sub>1.17</sub>Ge), or 25.0% (Fe<sub>1.25</sub>Ge), respectively. In each case, the calculation successfully converged to a local energy minimum, and the excess Fe atom(s) were located near Fe-sparse layers. This supports our ALMBE design to deposit excess Fe into the Fe-sparse layers. Regarding

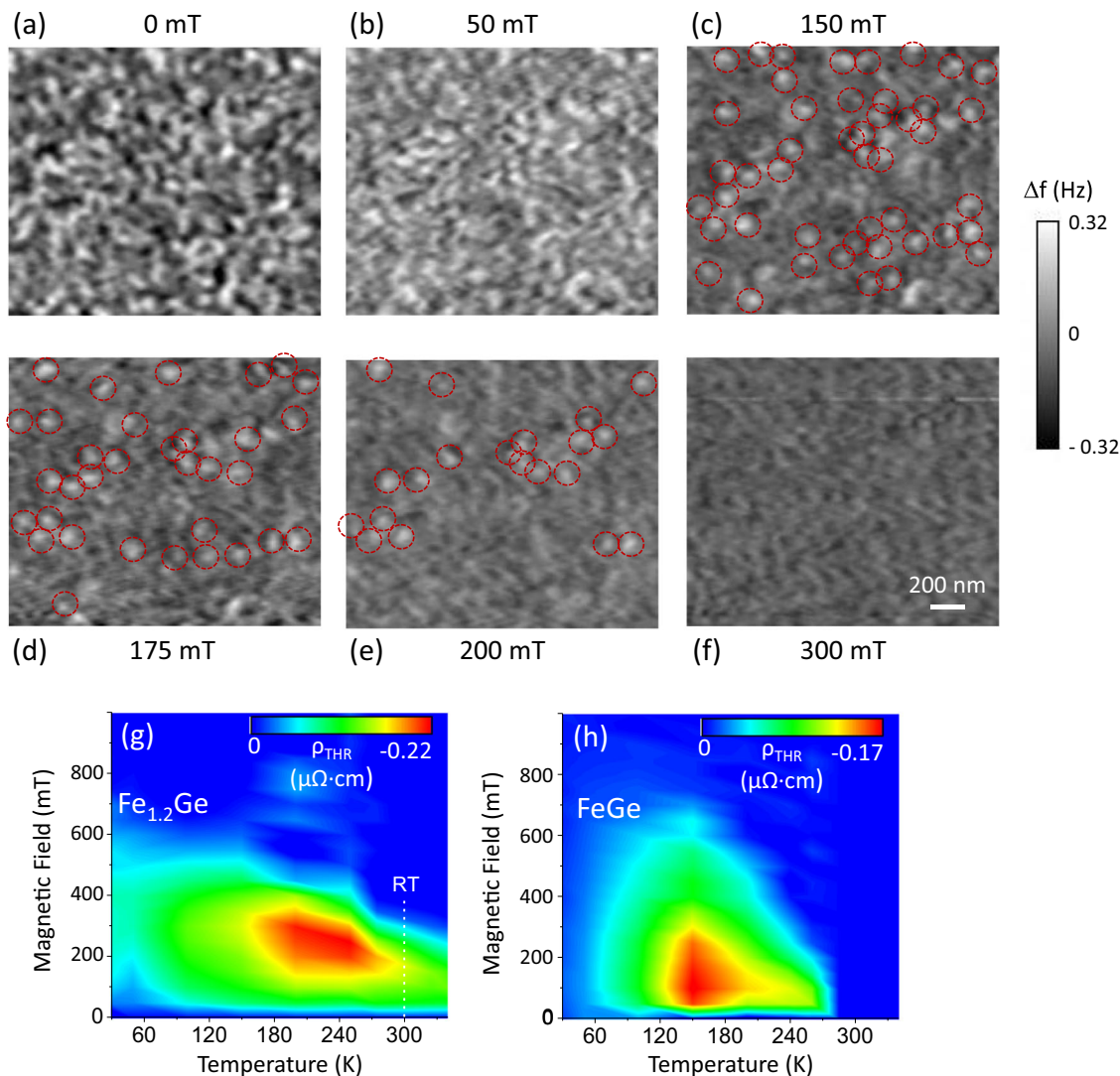


**Fig. 3 Magnetic force microscopy (MFM) imaging and topological Hall effect.** Room temperature MFM images of a 108 nm  $\text{Fe}_{1.2}\text{Ge}$  film, with out-of-plane magnetic fields of **a** 0 mT, **b** 50 mT, **c** 150 mT, **d** 175 mT, **e** 200 mT, **f** 300 mT. The shift in the frequency of the oscillating cantilever ( $\Delta f$ ) is proportional to the magnetic force gradient. Topological Hall resistivity for **g** Fe-rich  $\text{Fe}_{1.2}\text{Ge}$  and **h** FeGe. Red dashed circles identify skyrmions. MFM images without circles are provided in Figure S8 of Supplementary Note 2.

the HAADF image, since there are multiple sites for excess Fe and the site selection is subject to randomness (layer and position within layer), the imaging through the cross-section (e.g., an atom in the HAADF image is generated by a column of aligned atoms) combined with randomness causes the excess Fe atoms to average away. An extended discussion of the DFT results is included in the Supplementary Note 1

Magnetic properties investigated by SQUID magnetometry show an enhanced temperature dependence for Fe-rich  $\text{Fe}_{1.2}\text{Ge}$  compared to conventional FeGe. Applying a 2 Tesla out-of-plane field to remove any spin texture, the temperature scan shows that the field-polarized magnetization persists to above 400 K for Fe-rich  $\text{Fe}_{1.2}\text{Ge}$  (Fig. 2e, red curve) while the magnetization disappears at  $\sim 300$  K for FeGe (Fig. 2e, blue curve).

**MFM imaging of skyrmions.** Direct imaging of room-temperature skyrmions in Fe-rich  $\text{Fe}_{1.2}\text{Ge}$  was realized by MFM with a high-resolution tip and LTEM. Figure 3 shows room temperature MFM images obtained from a 108 nm thick Fe-rich  $\text{Fe}_{1.2}\text{Ge}$  film for different out-of-plane fields (see Methods for details of the measurement). At low magnetic fields of 0 mT and

50 mT (Fig. 3a, b), the magnetic domain structure consists of disordered stripes in white (i.e., helical phase) and a few white dots (i.e., skyrmions). As the magnetic field is increased to 150 mT (Fig. 3c), the stripes disappear and give way to the formation of many discontinuous dots. With further increasing field (Fig. 3d–f), the dots gradually disappear until they are virtually gone at 300 mT. This trend of magnetic domain structure as a function of the magnetic field is very similar to what has been observed in FeGe and other B20 skyrmion materials<sup>12,13,16,18,28</sup>.

**Topological Hall effect.** The topological Hall effect is another method often used to characterize the presence of skyrmions, as the topological Hall resistivity (THR) is theoretically predicted to be proportional to the skyrmion density. We determine the THR following the procedure outlined in Supplementary Note 3. Figure 3g shows the THR for Fe-rich  $\text{Fe}_{1.2}\text{Ge}$  as a function of out-of-plane magnetic field and temperature. For comparison, we measure the THR for pure FeGe (Fig. 3h), which has been studied previously<sup>13,16–18</sup>. We find the general features of the THR phase diagrams for Fe-rich  $\text{Fe}_{1.2}\text{Ge}$  and pure FeGe to be similar: the THR exhibits similar magnitudes, maxima occur at the finite



field, and the signal reduces at low temperatures. However, the THR for Fe-rich  $\text{Fe}_{1.2}\text{Ge}$  extends to much higher temperatures with substantial magnitude even at 340 K (the high-temperature limit of our instrument). These similarities suggest that the white dots observed in the room temperature MFM images are skyrmions, as the presence of skyrmions in pure FeGe is well established.

The measurement of THR and MFM provides the opportunity for a quantitative comparison, as both THR and MFM can be performed on as-grown samples without substrate removal. A detailed discussion is provided in Supplementary Note 4. Briefly, the skyrmion density and the THR have qualitative similarities such as having maximum values at 150 mT and decreasing as the field is increased above 150 mT. However, we do not observe a quantitative agreement in the field dependence, as the THR is not found to be proportional to the skyrmion density. In addition, in Supplementary Note 5, we estimate the magnitude of THR using a Drude model analysis<sup>29</sup> and obtain values that differ by a factor of 2–4 from the experimental values.

**LTEM imaging of skyrmions.** To determine the skyrmion sizes, we studied  $\text{Fe}_{1.2}\text{Ge}$  films using LTEM in the plan view. The LTEM raw images are strongly influenced by diffraction contrast (e.g., from grain boundaries). In order to enhance the magnetic contrast, as shown in Fig. 4a–c, we use a background subtraction procedure described in the Methods. The magnetic contrast observed for Fe-rich  $\text{Fe}_{1.2}\text{Ge}$  is similar to that observed previously in pure FeGe using similar methods<sup>26,27</sup>, further supporting the identification of the disordered stripes as helical textures and the

localized spin textures as skyrmions. The change in magnetic contrast in LTEM as a function of the applied field is consistent with the MFM results. At low magnetic fields, magnetic textures are stronger and randomly distributed as stripes and dots (Fig. 4a); while most of them fade off with the increase of magnetic fields, as shown in Fig. 4b, c. In LTEM, Bloch-type skyrmions appear as either bright or dark dots depending on their chirality<sup>27,30</sup>. To measure the size of the skyrmions, we selected and averaged the bright skyrmions circled in red in Fig. 4b, which were among the smallest observed and that clearly disappeared in Fig. 4c. The averaged skyrmion size is identified to be ~15 nm at room temperature (Fig. 4d).

**Micromagnetic parameters.** Finally, we discuss the micromagnetic parameters leading to the spin texture: saturation magnetization  $M_s$ , exchange stiffness  $A_{ex}$ , bulk DMI  $D$ , magnetic anisotropy  $K_u$ , and the Gilbert damping  $\alpha$ . One of the key questions in skyrmion materials is: what parameters determine the size and stability of skyrmions? The simplest answer is that the size of skyrmions is determined by the ratio of the exchange to DMI, namely by the length scale  $L_D = 4\pi A_{ex}/D$ <sup>31,32</sup>. However, there are several theoretical studies, especially of isolated skyrmions, which conclude that their size is *not* determined by  $L_D$ , and that it depends in an essential way on  $K_u$  and  $M_s$ <sup>33–35</sup>. In view of this, it is especially important to understand the parameters that characterize small, room-temperature skyrmions in Fe-rich FeGe. As discussed in detail in Supplementary Note 2, the combination of micromagnetic simulations with our experimental measurements (magnetization, ferromagnetic resonance,

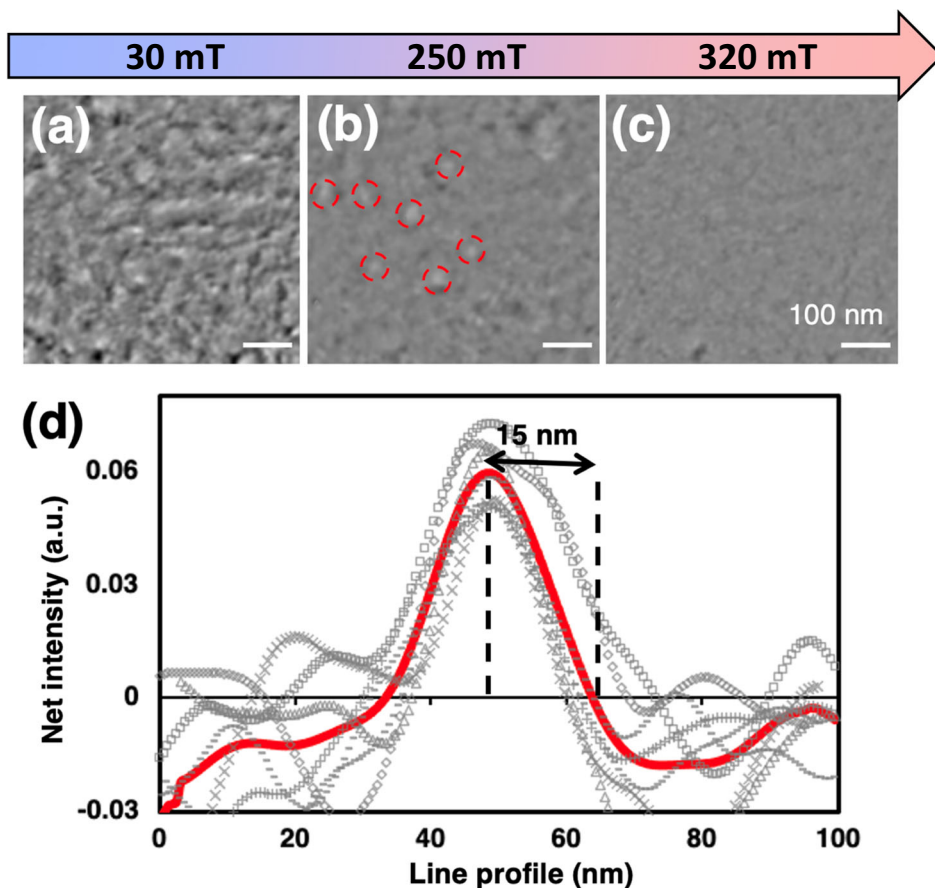


**Fig. 4 Lorentz transmission electron microscopy (LTEM) imaging.** Plan-view LTEM images, after removing the background, of a 108 nm  $\text{Fe}_{1.2}\text{Ge}$  film acquired at room temperature with out-of-plane magnetic fields: **a** 30 mT, **b** 250 mT, and **c** 320 mT. **d** The line profiles of the magnetic skyrmions are highlighted with red dashed circles in **(b)**. The red curve is an average of the line profiles.

MFM and LTEM) shows that the size of Bloch skyrmions is indeed determined by  $L_D \sim A_{ex}/D$  and weakly dependent of  $K_u$  and  $M_s$ . Quantitative estimates of the micromagnetic parameters are provided in Supplementary Note 6.

## Conclusions

In conclusion, the highly-controlled nonequilibrium synthesis of Fe-rich  $\text{Fe}_{1.2}\text{Ge}$  by RT-ALMBE has produced small skyrmions at room temperature in an epitaxial film. The incorporation of excess Fe into FeGe pushes the Curie temperature over room temperature, and MFM, LTEM, and THR identify RT skyrmions with a mean diameter as small as  $\sim 15$  nm. The realization of small skyrmions at room temperature is significant for the development of ultrahigh density, low-power magnetic memories.

## Methods

**Epitaxial growth.** Epitaxial FeGe and  $\text{Fe}_{1.2}\text{Ge}$  films were grown on Si(111) substrates in an MBE chamber with a base pressure of  $2 \times 10^{-10}$  Torr. Si(111) substrates were prepared by sonicating in acetone for 5 min and isopropyl alcohol for 5 min. The cleaned wafers were dipped in buffered HF for 2 min to remove the native oxide and terminate the dangling Si bonds with H, then rinsed in DI water. The substrates were immediately mounted onto Ta flag-style paddles, inserted into the growth chamber, and annealed at  $800^\circ\text{C}$  for 20 min to desorb the hydrogen to obtain a  $7 \times 7$  reconstruction. Thermal effusion cells were used for the deposition of Fe and Ge with the typical elemental growth rates in the range of  $1\text{--}4 \text{ \AA min}^{-1}$ . In situ, RHEED was used to monitor the crystallographic structure and atomic-scale roughness of the surface during growth. All samples began with a buffer layer of FeGe grown at  $300^\circ\text{C}$ , using co-deposition of Fe and Ge flux matched with a 1:1 ratio.

**Magnetic force microscopy.** MFM measurements were performed in a Quantum Design PPMS system to provide variable magnetic fields and temperatures. An MFM insert and high-resolution tips were used to probe the Fe-rich FeGe films. The MFM images were acquired in a constant height mode for a series of magnetic fields. In order to obtain the magnetic contribution to the frequency shifts, we subtracted the background signal<sup>36</sup> obtained by imaging at a high magnetic field of 1.5 T where the sample is magnetically saturated.

**Transmission electron microscopy.** The TEM investigations were carried out using a Thermo Scientific Image TITAN G2 60-300 microscope equipped with a Lorentz lens and image corrector, operated at 300 kV. The plan view TEM specimens were prepared from a  $\text{Fe}_{1.2}\text{Ge}$  (108 nm) thin film on FeGe buffer grown on Si(111) substrate using a wedge mechanical polishing method. The cross-section TEM specimens for HAADF-STEM characterization and XEDS analyses were prepared by a Ga-focused ion beam (FIB). The STEM XEDS spectrum imaging was performed using quad-silicon drift detectors, and the line profile of the elements ratio was measured along with the sample growth direction. Element ratio was normalized using the FeGe buffer layer as a reference, assuming  $\text{Fe/Ge} = 1$ .

LTEM images were taken with a defocus of  $100 \mu\text{m}$  to observe the magnetic contrast. The applied vertical magnetic field was controlled by varying the objective lens current of TEM. The actual magnetic fields were calibrated by a home-built TEM holder with a Hall-effect sensor. In our thin films, strong diffraction contrast is observed in LTEM mode, which reduces the visibility of magnetic contrast contributions. In order to reduce the diffraction contrast contributions in the LTEM image, we first recorded a series of LTEM images from the same

region of interest at different magnetic fields. Then, the LTEM image recorded at 360 mT, considering the sample is saturated and no magnetic contrast is present at that field, was subtracted as “background” contrast from all other images after some careful alignments and intensity normalization. More details of a similar procedure to enhance the magnetic contrast could be found in our earlier reports in a FeGe thin film plan view specimen<sup>26,27</sup>. In addition, Gaussian blurring of 4-pixel standard deviation ( $\sim 6$  nm) was performed to remove high-frequency noise in the background-removed LTEM images. The skyrmion size is measured from the FWHM of a line profile.

**Density functional theory.** Ab initio electronic structure calculations were carried out in the DFT framework using the plane-wave pseudopotential Quantum ESPRESSO code<sup>37</sup>. Core and valence electrons were treated using the ultrasoft pseudopotential method<sup>38</sup>. The exchange-correlation functionals were described using the Perdew–Burke–Ernzerhof parameterization of the generalized gradient approximation modified for solids (PBEsol<sup>39</sup>). To emulate the effects of epitaxial thin film growth the structure was oriented in a (111)-crystallographic plane. In addition, bulk structures were also considered for comparative studies. In the case of simulations involving (111)-oriented FeGe, excess Fe-atoms were added to the structure, which was then allowed to relax by expanding the unit cell only in the z-direction until an energy convergence threshold of  $10^{-8}$  eV and Hellmann–Feynman forces less than  $2 \text{ meV \AA}^{-1}$  were achieved. The plane wave cutoff energy was set to 60 Ry, the charge density cutoff was set at 600 Ry, and a  $\Gamma$ -centered Monkhorst–Pack  $k$ -point mesh with dimensions  $6 \times 6 \times 6$  was used to sample the Brillouin Zone. The Brillouin zone integration used Marzari–Vanderbilt smearing<sup>40</sup> with a smearing width of 0.27 eV. The scalar relativistic pseudopotentials were taken from the PSLibrary<sup>41</sup>. A collinear ferromagnetic spin order was imposed on all the Fe-atoms (including the interstitial Fe-atoms). Regardless of the initial position of the interstitial Fe-atoms, all structures relaxed to form a new Fe sparse layer in the structure. The converged out-of-plane lattice constant is  $9.5369 \text{ \AA}$ .

## Data availability

The datasets generated during and/or analyzed during the current study are available from the authors at reasonable request.

Received: 2 August 2023; Accepted: 31 October 2023;

Published online: 14 November 2023

## References

1. Fert, A., Cros, V. & Sampaio, J. Skyrmions on the track. *Nat. Nanotechnol.* **8**, 152–156 (2013).
2. Wiesendanger, R. Nanoscale magnetic skyrmions in metallic films and multilayers: a new twist for spintronics. *Nat. Rev. Mater.* **1**, 1–11 (2016).
3. Fert, A., Reyren, N. & Cros, V. Magnetic skyrmions: advances in physics and potential applications. *Nat. Rev. Mater.* **2**, 1–15 (2017).
4. Jiang, W. et al. Skyrmions in magnetic multilayers. *Phys. Rep.* **704**, 1–49 (2017).
5. Back, C. et al. The 2020 skyrmionics roadmap. *J. Phys. D* **53**, 363001 (2020).
6. Everschor-Sitte, K., Masell, J., Reeve, R. M. & Kläui, M. Perspective: magnetic skyrmions—overview of recent progress in an active research field. *J. Appl. Phys.* **124**, 240901 (2018).
7. Caretta, L. et al. Fast current-driven domain walls and small skyrmions in a compensated ferrimagnet. *Nat. Nanotechnol.* **13**, 1154–1160 (2018).
8. Mühlbauer, S. et al. Skyrmion lattice in a chiral magnet. *Science* **323**, 915–919 (2009).

9. Adams, T. et al. Long-range crystalline nature of the skyrmion lattice in MnSi. *Phys. Rev. Lett.* **107**, 217206 (2011).
10. Nii, Y. et al. Uniaxial stress control of skyrmion phase. *Nat. Commun.* **6**, 8539 (2015).
11. Li, Y. et al. Robust formation of skyrmions and topological hall effect anomaly in epitaxial thin films of MnSi. *Phys. Rev. Lett.* **110**, 117202 (2013).
12. Yu, X. Z. et al. Near room-temperature formation of a skyrmion crystal in thin-films of the helimagnet FeGe. *Nat. Mater.* **10**, 106–109 (2011).
13. Huang, S. X. & Chien, C. L. Extended skyrmion phase in epitaxial FeGe(111) thin films. *Phys. Rev. Lett.* **108**, 267201 (2012).
14. Zhang, L. et al. Critical phenomenon of the near room temperature skyrmion material FeGe. *Sci. Rep.* **6**, 22397 (2016).
15. Kovács, A. et al. Mapping the magnetization fine structure of a lattice of Bloch-type skyrmions in an FeGe thin film. *Appl. Phys. Lett.* **111**, 192410 (2017).
16. Gallagher, J. C. et al. Robust zero-field skyrmion formation in FeGe epitaxial thin films. *Phys. Rev. Lett.* **118**, 027201 (2017).
17. Leroux, M. et al. Skyrmion lattice topological Hall effect near room temperature. *Sci. Rep.* **8**, 15510 (2018).
18. Ahmed, A. S. et al. Chiral bobbers and skyrmions in epitaxial FeGe/Si(111) films. *Phys. Rev. Mater.* **2**, 041401(R) (2018).
19. Kanazawa, N. et al. Large topological Hall effect in a short-period helimagnet MnGe. *Phys. Rev. Lett.* **106**, 156603 (2011).
20. Tanigaki, T. et al. Real-space observation of short-period cubic lattice of skyrmions in MnGe. *Nano Lett.* **15**, 5438–5442 (2015).
21. Balasubramanian, B. et al. Chiral magnetism and high-temperature skyrmions in B20-ordered Co-Si. *Phys. Rev. Lett.* **124**, 057201 (2020).
22. Budhathoki, S. et al. Room-temperature skyrmions in strain-engineered FeGe thin films. *Phys. Rev. B* **101**, 220405 (2020).
23. Dzyaloshinsky, I. A thermodynamic theory of “weak” ferromagnetism of antiferromagnetics. *J. Phys. Chem. Solids* **4**, 241–255 (1958).
24. Moriya, T. Anisotropic superexchange interaction and weak ferromagnetism. *Phys. Rev.* **120**, 91–98 (1960).
25. Corbett, J. P. et al. Determining surface terminations and chirality of noncentrosymmetric FeGe thin films via scanning tunneling microscopy. *ACS Appl. Mater. Interfaces* **12**, 9896–9901 (2020).
26. Bagues, N. et al. Imaging of magnetic textures in polycrystalline FeGe thin films via in-situ Lorentz transmission electron microscopy. *Microsc. Microanal.* **26**, 1700–1702 (2020).
27. Wang, B., Bagues, N., Liu, T., Kawakami, R. K. & McComb, D. W. Extracting weak magnetic contrast from complex background contrast in plan-view FeGe thin films. *Ultramicroscopy* **232**, 113395 (2022).
28. Kanazawa, N., Shibata, K. & Tokura, Y. Variation of spin-orbit coupling and related properties in skyrmionic system  $Mn_{1-x}Fe_xGe$ . *N. J. Phys.* **18**, 045006 (2016).
29. Bruno, P., Dugaev, V. K. & Taillefumier, M. Topological Hall effect and Berry phase in magnetic nanostructures. *Phys. Rev. Lett.* **93**, 096806 (2004).
30. Nguyen, K. X. et al. Disentangling magnetic and grain contrast in polycrystalline FeGe thin films using four-dimensional Lorentz scanning transmission electron microscopy. *Phys. Rev. Appl.* **17**, 034066 (2022).
31. Nagaosa, N. & Tokura, Y. Topological properties and dynamics of magnetic skyrmions. *Nat. Nanotechnol.* **8**, 899–911 (2013).
32. Banerjee, S., Rowland, J., Erten, O. & Randeria, M. Enhanced stability of skyrmions in two-dimensional chiral magnets with Rashba spin-orbit coupling. *Phys. Rev. X* **4**, 031045 (2014).
33. Büttner, F., Lemesch, I. & Beach, G. S. D. Theory of isolated magnetic skyrmions: From fundamentals to room temperature applications. *Sci. Rep.* **8**, 4464 (2018).
34. Wang, X. S., Yuan, H. Y. & Wang, X. R. A theory on skyrmion size. *Commun. Phys.* **1**, 1–7 (2018).
35. Bera, S. & Mandal, S. S. Theory of the skyrmion, meron, antiskyrmion, and antimeron in chiral magnets. *Phys. Rev. Res.* **1**, 033109 (2019).
36. Meng, K.-Y. et al. Observation of nanoscale skyrmions in SrIrO<sub>3</sub>/SrRuO<sub>3</sub> bilayers. *Nano Lett.* **19**, 3169–3175 (2019).
37. Giannozzi, P. et al. QUANTUM ESPRESSO: a modular and open-source software project for quantum simulations of materials. *J. Phys.* **21**, 395502 (2009).
38. Vanderbilt, D. Soft self-consistent pseudopotentials in a generalized eigenvalue formalism. *Phys. Rev. B* **41**, 7892–7895 (1990).
39. Perdew, J. P. et al. Restoring the density-gradient expansion for exchange in solids and surfaces. *Phys. Rev. Lett.* **100**, 136406 (2008).
40. Marzari, N., Vanderbilt, D., De Vita, A. & Payne, M. C. Thermal contraction and disordering of the Al(110) surface. *Phys. Rev. Lett.* **82**, 3296–3299 (1999).
41. Dal Corso, A. Pseudopotentials periodic table: from H to Pu. *Comput. Mater. Sci.* **95**, 337–350 (2014).

## Acknowledgements

This work was supported by the DARPA TEE program under Grants Nos. D18AP00008 and D18AP00009. This research was partially supported by the Center for Emergent Materials, an NSF MRSEC, under award number DMR-2011876.

## Author contributions

T.L., R.A.B., S.C., and R.K.K. performed the MBE growth, SQUID, XRD, and THR measurements. C.M.S., J.P.C., J.R.R., and J.A.G. performed the MFM measurements and analysis. B.W., N.B., and D.W.M. performed the STEM and LTEM measurements and analysis. T.Q.H., P.V.B., D.P., P.K.W., and M.R. performed the theoretical analysis. B.M. and P.C.H. performed the FMR measurements. All authors contributed to the preparation of the paper.

## Competing interests

The authors declare no competing interests.

## Additional information

**Supplementary information** The online version contains supplementary material available at <https://doi.org/10.1038/s42005-023-01444-1>.

**Correspondence** and requests for materials should be addressed to Roland K. Kawakami.

**Peer review information** *Communications Physics* thanks the anonymous reviewers for their contribution to the peer review of this work.

**Reprints and permission information** is available at <http://www.nature.com/reprints>

**Publisher's note** Springer Nature remains neutral with regard to jurisdictional claims in published maps and institutional affiliations.



**Open Access** This article is licensed under a Creative Commons Attribution 4.0 International License, which permits use, sharing, adaptation, distribution and reproduction in any medium or format, as long as you give appropriate credit to the original author(s) and the source, provide a link to the Creative Commons license, and indicate if changes were made. The images or other third party material in this article are included in the article's Creative Commons license, unless indicated otherwise in a credit line to the material. If material is not included in the article's Creative Commons license and your intended use is not permitted by statutory regulation or exceeds the permitted use, you will need to obtain permission directly from the copyright holder. To view a copy of this license, visit <http://creativecommons.org/licenses/by/4.0/>.

© The Author(s) 2023